Ceramics International 45 (2019) 17192–17203

Contents lists available at ScienceDirect

Ceramics International

journal homepage: www.elsevier.com/locate/ceramint

Flower-like $NiCo_2O_4/NiCo_2S_4$ electrodes on Ni mesh for higher supercapacitor applications

S.K. Shinde[a], M.B. Jalak[b], G.S. Ghodake[a], N.C. Maile[b], H.M. Yadav[c], A.D. Jagadale[d], Asif Shahzad[e], D.S. Lee[e], A.A. Kadam[f], V.J. Fulari[b], D.-Y. Kim[a,*]

[a] Department of Biological and Environmental Science, College of Life Science and Biotechnology, Dongguk University, 32 Dongguk-ro, Biomedical Campus, Ilsandong-gu, Siksa-dong, 10326, Goyang-si, Gyeonggi-do, South Korea
[b] Department of Physics, Shivaji University, Kolhapur, 416004, Maharashtra, India
[c] Department of Energy and Materials Engineering, Dongguk University, Seoul, 04620, South Korea
[d] Department of Electrical and Electronics Engineering, School of Electrical and Electronics Engineering, SASTRA Deemed University, Thanjavur, 613401, Tamilnadu, India
[e] Department of Environmental Engineering, Kyungpook National University, 80 Daehak-ro, Buk-gu, Daegu, 41566, South Korea
[f] Research Institute of Biotechnology and Medical Converged Science, Dongguk University, Biomedi Campus, Ilsandong-gu, Goyang-si, Gyeonggi-do, 10326, Republic of Korea

ARTICLE INFO

Keywords:
$NiCo_2O_4/NiCo_2S_4$ electrodes
Nanoflower
Co-precipitation
Screen printing method
Specific capacitance

ABSTRACT

In this research, we have effectively synthesized a novel $NiCo_2O_4/NiCo_2S_4$ powder by co-precipitation and thin films prepared using a screen-printing method on Ni mesh for supercapacitor applications. Herein, we report the effect of unique hierarchical nanostructures and the systematic effect of Ni and Co on the structural, morphological and electrical properties of the $NiCo_2O_4/NiCo_2S_4$ electrodes. The optimized $NiCo_2O_4/NiCo_2S_4$ electrode shows outstanding performance with a specific capacitance of 1966 $F\,g^{-1}$ at 5 $mV\,s^{-1}$. The cycling stability reports indicate the $NiCo_2O_4/NiCo_2S_4$ electrodes have an outstanding cyclic stability with 91% capacity retention. From the supercapacitor performance results, we confirmed that the $NiCo_2O_4/NiCo_2S_4$ electrode is useful for the fabrication of symmetric supercapacitors. These results reveal that the $NiCo_2O_4/NiCo_2S_4$ electrodes is a capable electrode material for supercapacitor applications in the future.

1. Introduction

In recent years, with the growth of the world economy, society has demanded electrical energy storage devices with high power and energy densities for use with alternative energy sources [1]. In recent years, many electrical energy storage devices are available in the market. Out of these, supercapacitors receive great consideration due to their low-cost, high power and energy densities [1,2], excellent stability [3], and fast charge-discharge compared to lithium-ion batteries and traditional capacitors [4]. Anodic and cathodic materials play an important role in the storage of electrical energy in supercapacitors [1–5]. However, the main problem in commercial device fabrication is lower power and energy density in supercapacitors [5]. Specific capacitance and cycling performance of supercapacitors can be enhanced by changing working materials. This is an important factor, which is beneficial for commercial applications of supercapacitors [6]. The main key is developing new strategies to improve energy storage with higher specific capacitance and long cyclic stability [7].

Currently, binary and ternary transition metal oxides are used for higher theoretical and experimental specific capacitance, which are very useful for portable electronic device fabrication [8]. However, transition metal oxides have comparatively lower electrical conductivity and low cyclic stability [9]. To avoid these problems, we apply a new strategy to design new nanostructure composite materials that have higher electrical conductivity and device performance [10,11]. Binary and ternary metal sulfides, like NiS, CoS and $NiCo_2S_4$, demonstrate better performance in various fields, such as oxygen evolution reactions [12], supercapacitors [13], water splitting [14], photocatalytic hydrogen evolution [15], and dye-sensitized solar cells [16], etc., than other oxides and hydroxides, for example NiO, CoO, $Co(OH)_2$, $Ni(OH)_2$, $MnCo_2O_4/CoCo_2O_4$, Mn:Co_3O_4, and $ZnCo_2O_4$ thin films [17–19]. Out of these ternary transition metal sulfides, $NiCo_2S_4$ and $NiCo_2O_4$ electrodes are better for supercapacitor application, because they provide higher electrical conductivity, high surface area, have excellent capacitive properties, and are environmentally stable [20–22].

* Corresponding author.
E-mail address: sbpkim@dongguk.edu (D.-Y. Kim).

https://doi.org/10.1016/j.ceramint.2019.05.274
Received 5 February 2019; Received in revised form 25 April 2019; Accepted 23 May 2019
Available online 25 May 2019

Currently, researchers are focusing on improving electrode performance. So, we use a novel approach to prepare a new composite thin film of transition metal sulfide/oxide to increase the supercapacitor performance. There are several researchers that have reported on composite thin films for supercapacitor application. For example, Liu et al. [23] successfully prepared hybrid composite thin films of $NiCo_2O_4$–$NiCo_2S_4$ using NiCo bimetallic ZIFs as solid precursors. They reported a 1296 F g^{-1} specific capacitance at a 1 mA cm^{-1} current density. Raj et al. [24] produced a mixed ternary $NiCo_2O_4$/$NiCo_2S_4$ hybrid material on Ni foam using an evaporation technique. They mentioned that the $NiCo_2O_4$/$NiCo_2S_4$ hybrid electrodes show significant supercapacitive performance compared to without the composite of $NiCo_2O_4$ and $NiCo_2S_4$. Jinlong et al. [25] synthesized $NiCo_2S_4$ nanotubes on Ni foam of NiCo by a hydrothermal method. The nanotube-like $NiCo_2S_4$ electrode demonstrated a higher capacitance value of 1936.2 F g^{-1} and excellent stability after 5000 cycles. Rong et al. [26] prepared $NiCo_2O_4$@$NiCo_2S_4$ hybrid thin films with a multistep method. First, he deposited $NiCo_2O_4$ nanowires on Ni foam using a hydrothermal method and then deposited $NiCo_2O_4$ on the $NiCo_2S_4$ using a vapor-phase hydrothermal method. The $NiCo_2O_4$@$NiCo_2S_4$ coated Ni substrate displays a maximum specific capacitance of 1872 F g^{-1} at 1 A g^{-1} current density. Preparation method is very important for the formation of 3D nanostructures. Several methods have been used to synthesize $NiCo_2O_4$@$NiCo_2S_4$ nanomaterials. The co-precipitation and screen-printing method is very easy, low-cost, useful, and gorgeous method. Screen printing has a very attractive deposition technique because the formation of nanostructures is by layer-by-layer deposition with a large surface area on the substrate. Screen printing is the best technique for the preparation of thin films for supercapacitor applications due to its short deposition time, higher deposition area, simply handling, and low cost. However, to the best of our knowledge, there are no reports on $NiCo_2O_4$/$NiCo_2S_4$ electrode production for supercapacitor application using the screen-printing method [27].

In this paper, we examine the synthesis of $NiCo_2O_4$/$NiCo_2S_4$ nanomaterials with different ratios of Ni and Co precursors and the characterization of as-synthesized and annealed $NiCo_2O_4$/$NiCo_2S_4$ with various 3D nanostructures, such as nanoflakes, nanoflowers, nanosheets, and microspheres using a simple, unique co-precipitation method and consequential supercapacitor applications. The $NiCo_2O_4$/$NiCo_2S_4$ thin films were characterized by physical, chemical and electrical properties, such as X-ray diffraction (XRD), field emission scanning electron microscopy (FE-SEM), transmission electron microscopy (TEM), cyclic voltammetry (CV), galvanostatic charge/discharge, and electrochemical impedance spectroscopy.

2. Experimental details

2.1. Materials

The chemicals used for the synthesis of $NiCo_2O_4$/$NiCo_2S_4$ power were 0.1 M nickel (II) sulfate ($NiSO_4{\cdot}6H_2O$), 0.1 M cobalt (II) sulfate ($CoSO_4{\cdot}7H_2O$), 0.2 M sodium sulfide ($Na_2S{\cdot}5H_2O$), ammonium hydroxide (NH_4OH), and polyvinyl alcohol.

2.2. Synthesis of $NiCo_2O_4$/$NiCo_2S_4$ thin films

In a typical synthesis process, 0.1 M $NiSO_4$ $6H_2O$, 0.1 M $CoSO_4$ $7H_2O$, and 0.2 M Na_2S $5H_2O$ were dissolved separately in 30 mL of double-distilled water. To produce an alkaline solution, liquid ammonia was added dropwise to Ni and Co precursors. Initially, precipitate observed and after some time it was dissolved. The pH of the Ni and Co precursor solution was maintained to 11. Then Ni and Co precursors were dropwise added to Na_2S solution. A black precipitate formed and continues forming for 1 h. The resulting powder was filtered and washed with distilled water and ethanol repeatedly for five times. The as-prepared powder was annealed at 300 °C for 1 h in air and subsequently used to prepare $NiCo_2O_4$/$NiCo_2S_4$ films via the screen-printing method and labeled as, NCS/O:3, NCS/O:4, and NCS/O:5.

2.3. Screen printing $NiCo_2O_4$/$NiCo_2S_4$ films

The chemical co-precipitation synthesized powder was used to make thin films of $NiCo_2O_4$/$NiCo_2S_4$ for supercapacitors. PVA gel was added dropwise to the powder and continuously ground up to a viscous paste. The appropriate amount of PVA was added to give a viscous paste for the homogenous and uniform printing of $NiCo_2O_4$/$NiCo_2S_4$ thin films on Ni mesh. The $NiCo_2O_4$/$NiCo_2S_4$ coated thin films were air dried for 6 h and air annealed at 200 °C for 2 h for the vaporization of water and other impurities. The active mass deposited on Ni mesh is 0.66 mg cm^{-2} for all prepared $NiCo_2O_4$/$NiCo_2S_4$ thin films. These prepared $NiCo_2O_4$/$NiCo_2S_4$ thin films were used to measure electrochemical properties with tests like CV, galvanostatic charge/discharge (GCD), and electrochemical impedance spectroscopy (EIS).

2.4. Characterization

The crystalline structures of the as-prepared and annealed samples were detected using a Rigaku Ultima III diffractometer operated at 40 kV and 30 mA with Cu K_α radiation (1.54 Å) as a source, with a scanning range of 2θ over 20–80°. The nanostructure of the as-prepared and annealed samples were examined by FE-SEM using a JEOL JSM-7100 and high-resolution TEM (HR-TEM; JEOL, Model JEM-2100). X-ray photoelectron spectroscopy (XPS; ULVAC-PHI Quantera SXM) was used to examine the elemental composition of as-synthesized samples fitted XPS data with CasaXPS version 2.3.18PR1.0 program [28,29].

2.5. Preparation and electrochemical testing of $NiCo_2O_4$/$NiCo_2S_4$ electrodes

The electrochemical properties were tested using as-synthesized $NiCo_2O_4$/$NiCo_2S_4$ thin film as a working electrode, which was synthesized at different Ni and Co volume percentages, as described elsewhere [29,30]. A three-electrode system, which included a $NiCo_2O_4$/$NiCo_2S_4$ electrode as the working electrode, Pt as the counter electrode, and an Ag/AgCl electrode as the reference electrode, was used to assess the electrochemical performance of the as-prepared $NiCo_2O_4$/$NiCo_2S_4$ electrodes. The working electrode probe was connected to a flexible $NiCo_2O_4$/$NiCo_2S_4$/Ni electrode. The reference electrode probe was connected to an Ag/AgCl electrode, and the counter electrode probe was connected to a thin Pt electrode. The working electrode probe, connected to the $NiCo_2O_4$/$NiCo_2S_4$/Ni flexible electrode, was immersed in a 2 M KOH electrolyte solution. The supercapacitor properties were tested in the $-0.2-0.5$ V potential window. EIS tests were performed between 1 and 100 kHz, with AC amplitude of 10 mV and bias potential of 0.34 V. In electrochemical testing experiments, CV, GCD, and EIS measurements were performed with a CHI 660E electrochemical workstation in aqueous 2 M KOH electrolyte [30].

2.6. Fabrication of flexible symmetric devices

The flexible symmetric $NiCo_2O_4$/$NiCo_2S_4$ thin films were assembled by using the optimized NCS/O:4 thin films as positive and negative electrodes. The both electrodes of NCS/O:4 thin films are separated using filter paper, and poly (vinyl alcohol) (PVA)/KOH gel was used as the electrolyte. We used similar process for the preparation of the PVA/KOH gel as reported previously [31]. The PVA/KOH gel was prepared by mixing 2 g KOH in 20 mL DDW and after dissolving, 2 g PVA added in the DDW. Further, adding the PVA, the solution was heated at 30 °C for 30 min under the constant stirring. The prepared both NCS/O:4 electrodes and separator paper were dipped into the gel electrolyte for 5 s, and then these electrodes were dried in air at 25 °C for 12 h. Finally, these electrodes were pressed by sandwiching separator in between at

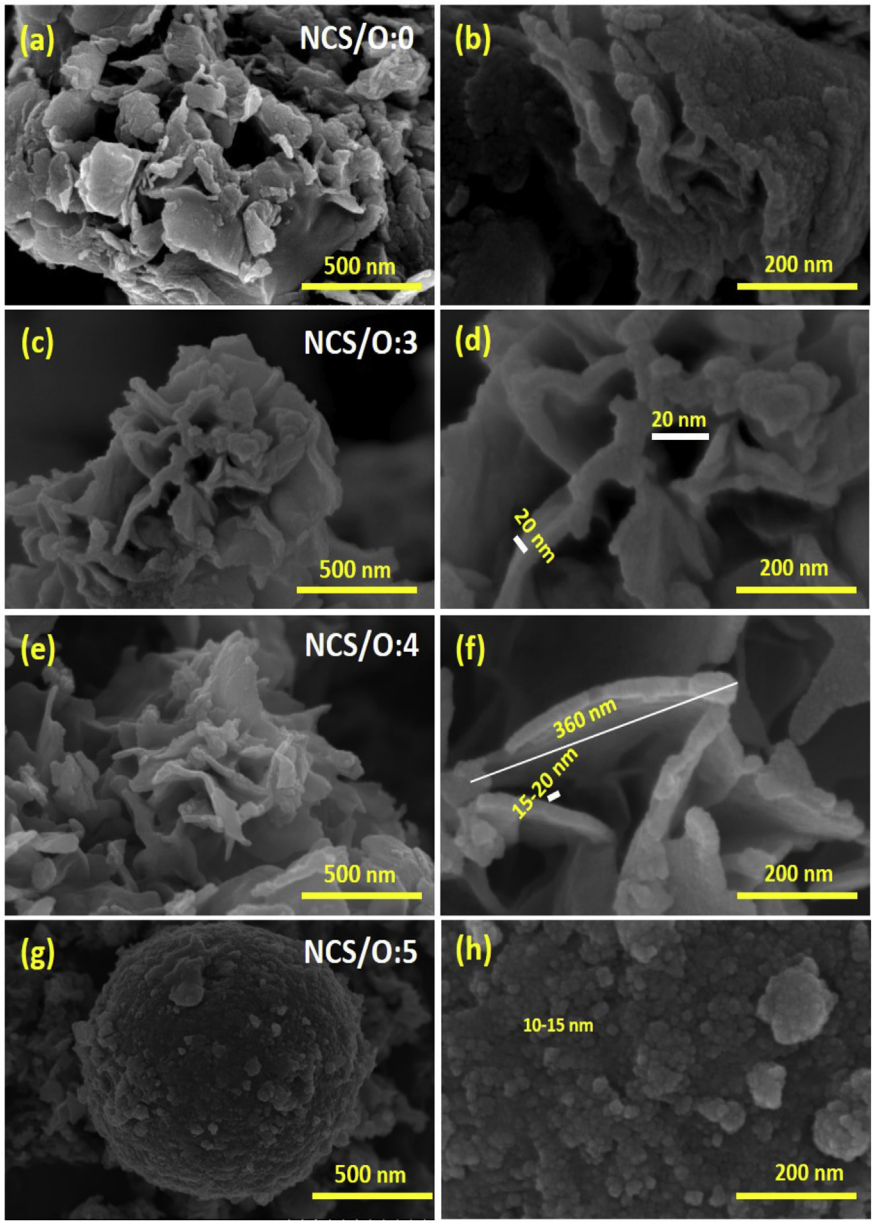

Fig. 1. FE-SEM images of (a, b) NCS/O:0, (c, d) NCS/O:3, (e, f) NCS/O:4, and (g, h) NCS/O:5 samples of the $NiCo_2O_4/NiCo_2S_4$ composites with different Ni and Co volume ratio with different magnification.

35 °C for 6 h.

3. Results and discussion

3.1. FE-SEM and TEM analysis

The surface morphology and the nanostructure of the as-prepared and annealed composites of $NiCo_2O_4/NiCo_2S_4$ were further characterized by FE-SEM. Fig. 1(a–h) shows the FE-SEM images of as-prepared and annealed composites of $NiCo_2O_4/NiCo_2S_4$ samples with different magnification. Fig. 1b shows sheets of honeycomb-like nanostructures with porous interconnected sheets, developing nano-holes with diameters average in the range 100–200 nm (Fig. 1a). At high magnification, the FE-SEM images show the nanoparticles are fully covered with porous surface area, and spherical size of individual particles is in the 10–20 nm range (Fig. 1b) [32]. After annealing samples at 300 °C, $NiCo_2O_4/NiCo_2S_4$ shows a drastic change in surface morphology from nanosheets to nanoflower-like nanostructures, which are composed of many interconnected flakes are shown in Fig. 1 (c, d). At careful observation, we observed that the sample surface shows the top-view of a rose flower. Fig. 1d shows a high magnification of a $NiCo_2O_4/NiCo_2S_4$ composite, which was synthesized at Ni (10%) and Co (30%) ratio by a co-precipitation method. The average thicknesses of the nanoplates are calculated as 20–25 nm with a highly porous surface (Fig. 1d) [33]. Upon further changing the composition of the Ni (10 → 20) and Co (30 → 20), the samples demonstrate a useful development in $NiCo_2O_4/NiCo_2S_4$ composites. It shows a surface that is highly uniform, fully covered, and interconnected with porous nanoflake-likes nanostructures shown in Fig. 1(e and f). These interconnected nanostructures are found to be more appropriate for the electrochemical application. The length of vertical nanoflakes range from 300 to 360 nm and the thickness 15–20 nm. The separation distance between these vertical, interconnected nanoflakes is around 100–200 nm. This separation gap is very useful for ion movement during the electrochemical testing [34]. Fig. 1 (g, h) shows the microspheres of $NiCo_2O_4/NiCo_2S_4$ composites at percentages of Ni and Co are 30 and 10, respectively. The diameter of a

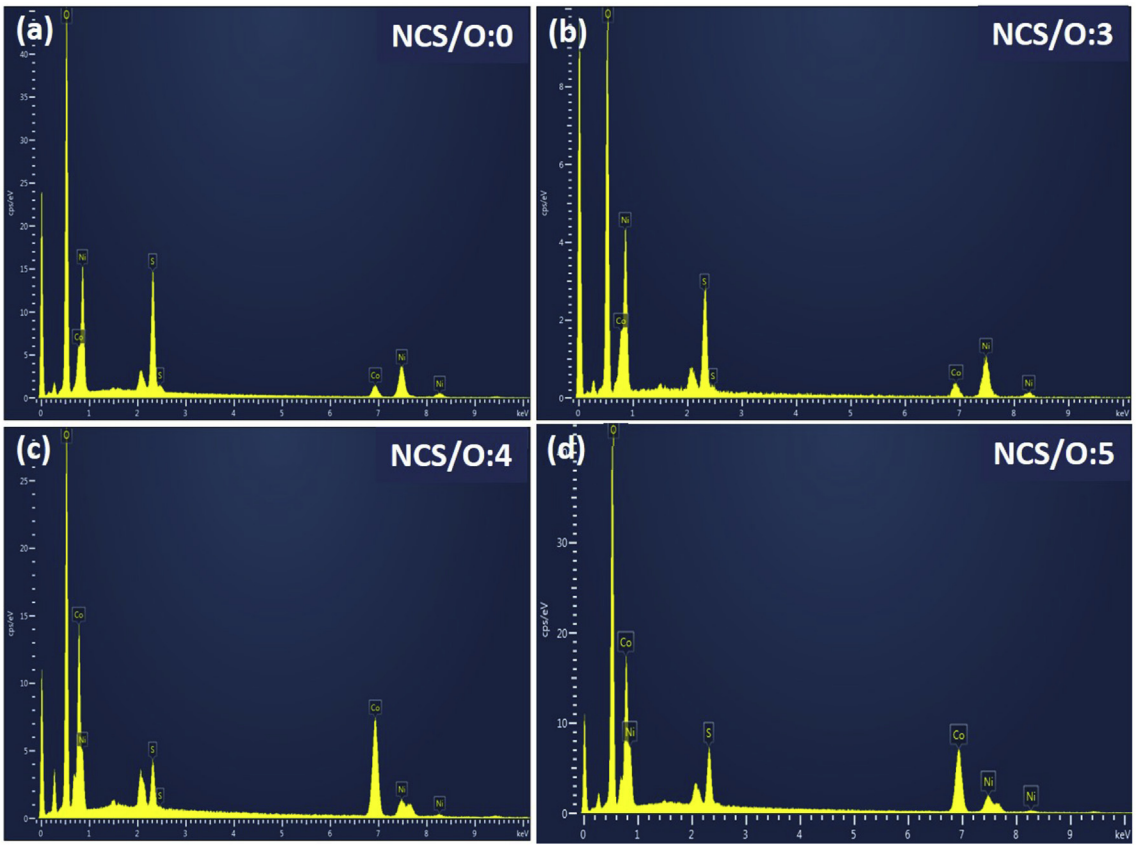

Fig. 2. EDS images of the (a) NCS/O:0, (b) NCS/O:3, (c) NCS/O:4, and (d) NCS/O:5 samples of the $NiCo_2O_4/NiCo_2S_4$ composites thin films.

microsphere is around 1.5–2 μm with a porous nanostructure. Fig. 1h shows a high magnification image and indicates the aggregation of nanoparticles with a 10–15 nm size [35]. An EDS investigation was used to study the composition of hybrid $NiCo_2O_4/NiCo_2S_4$ composite nanostructures. Fig. 2 shows that the nickel, cobalt, sulfur, and oxygen are present in the as-synthesized and annealed composites of the $NiCo_2O_4/NiCo_2S_4$ samples. From the XRD, XPS, FE-SEM and EDS results, we can confirm the formation of hybrid $NiCo_2O_4/NiCo_2S_4$ nanosheets that are composed of $NiCo_2S_4$ with nanosheets-like nanostructures.

Additional examinations of the morphology of as prepared and annealed hybrid $NiCo_2O_4/NiCo_2S_4$ composites sample were investigated by TEM. TEM images and elemental mapping of $NiCo_2O_4/NiCo_2S_4$ composites are shown in Fig. 3. Fig. 3(a–h) shows the TEM images of $NiCo_2O_4/NiCo_2S_4$ composites. From TEM analysis, we concluded that the annealed samples are highly porous and homogeneously dispersed on the carbon grid, out of the annealed samples, NCS/O:4 shows the high porosity nanoflake $NiCo_2O_4/NiCo_2S_4$ nanostructures, which are very useful for the electrochemical reaction because porous $NiCo_2O_4/NiCo_2S_4$ nanosheets provide more active sites and plentiful holes and void gaps between nanoflakes help the diffusion and penetration of ions and electrons during the electrochemical charge-discharge process [36]. Also, it provides excellent electrical conductivity for electron transportation. The inset shows the individual nanoflakes and nanoflower-like TEM images of sample NCS/O:4. It was clearly shown that the NCS/O:4 was superior for electrochemical applications due to its porosity and higher reactive area. The HR-TEM image presents two types of lattice fringes at 0.13 and 0.26 nm, matching the (400) and (311) planes of $NiCo_2O_4$ and $NiCo_2S_4$, respectively, which indicates the formation of hybrid $NiCo_2O_4/NiCo_2S_4$ nanocrystals. Fig. 4(a and b) shows the SAED pattern and HR-TEM of sample NCS/O:4 suggests that the formation of hybrid $NiCo_2O_4/NiCo_2S_4$ nanoflakes are polycrystalline with a cubic crystal structure, respectively [34,37].

3.2. XRD analysis

The crystallographic studies of the $NiCo_2O_4/NiCo_2S_4$ composite powder were carried out using XRD. Fig. 5A (a–d) shows the XRD patterns of as-synthesized and air annealed $NiCo_2O_4/NiCo_2S_4$ samples prepared by the co-precipitation method with different ratios of Ni and Co precursor. As synthesized composite powder was annealed at a temperature of 300 °C for 1 h. After annealing, we observed that $NiCo_2O_4/NiCo_2S_4$ composite shows a more intense and highly pure phase of $NiCo_2O_4/NiCo_2S_4$ compared to the as-synthesized composite powder [23,38]. Fig. 5A (b–c) shows the $NiCo_2O_4/NiCo_2S_4$ composite powder prepared with different ratios of Ni and Co. These peaks corresponded with the cubic phase of $NiCo_2S_4$ materials (JCPDS: 20-0782) and $NiCoO_4$ (JCPDS:20-0781) without any other impurities like NiO, CoS, NiS, and CoO [39]. The diffraction peaks at 31.30°, 36.00°, 55.57°, 65.0° are related to the (311), (400), (440) and (533) planes of the $NiCo_2S_4$ cubic crystal, respectively. The high-intensity peak at 36.73° is related to the (311) plain of $NiCo_2O_4$, which was confirmed by the standard result. The peaks located at 36.73°, 44.74°, and 59.24° matches with the (311), (400), and (511) planes of the $NiCo_2O_4$ sample [40]. After annealing, XRD results show the formation of a hybrid $NiCo_2S_4$ and $NiCo_2O_4$ phase using the co-precipitation method. The XRD results match well with previous reports [26,41].

3.3. Raman analysis

Raman spectroscopy was used to confirm the crystal structures of as-synthesized and annealed samples. Figure S1 (a–d) shows the Raman spectra of the $NiCo_2O_4/NiCo_2S_4$ composite materials synthesized using the co-precipitation method, and provide strong evidence for the

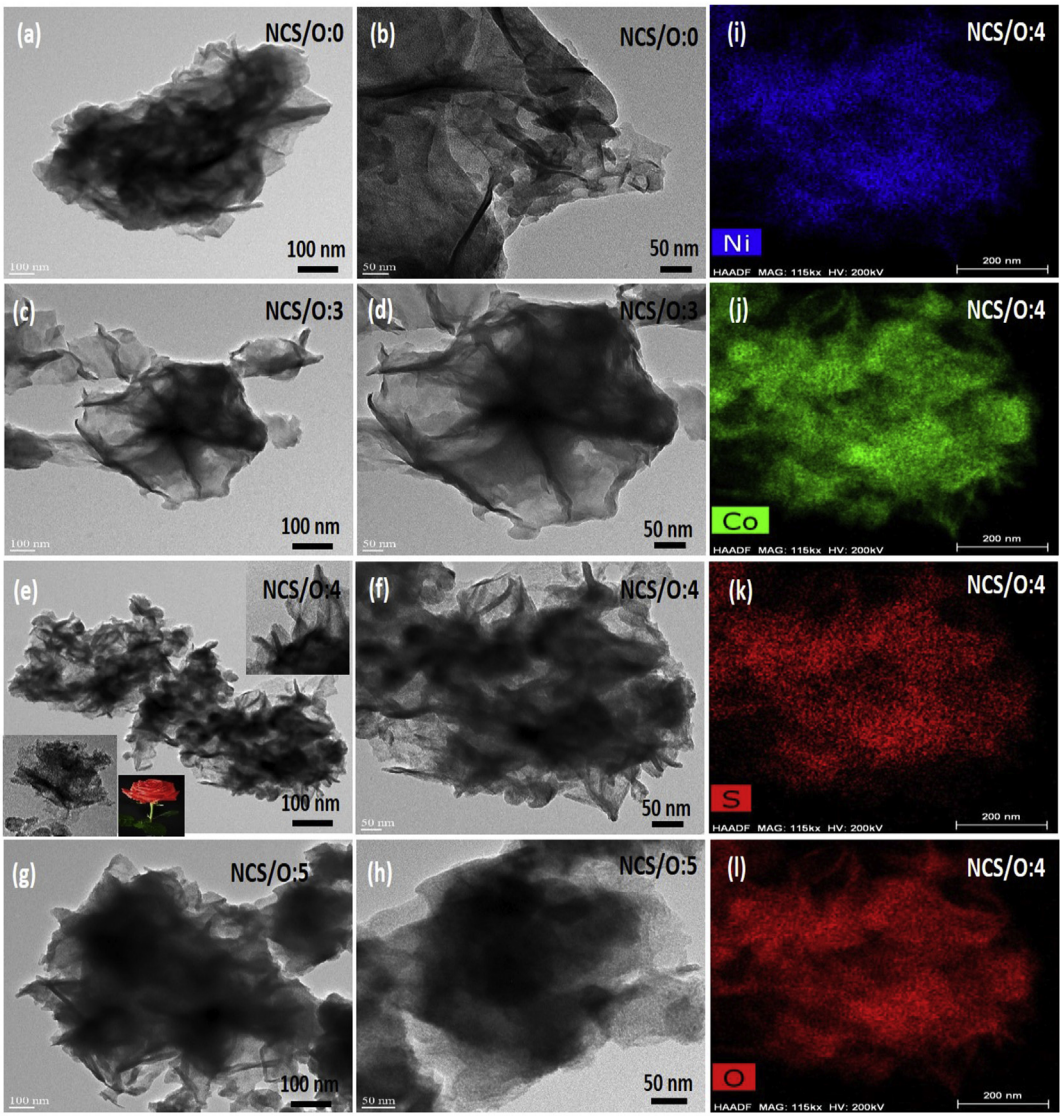

Fig. 3. TEM images of the (a, b) NCS/O:0, (c, d) NCS/O:3, (e, f) NCS/O:4, and (g, h) NCS/O:5 samples of the $NiCo_2O_4/NiCo_2S_4$ composites by co-precipitation method with different magnification and (i–l) Elemental mapping of optimized NCS/O:4 composites, respectively.

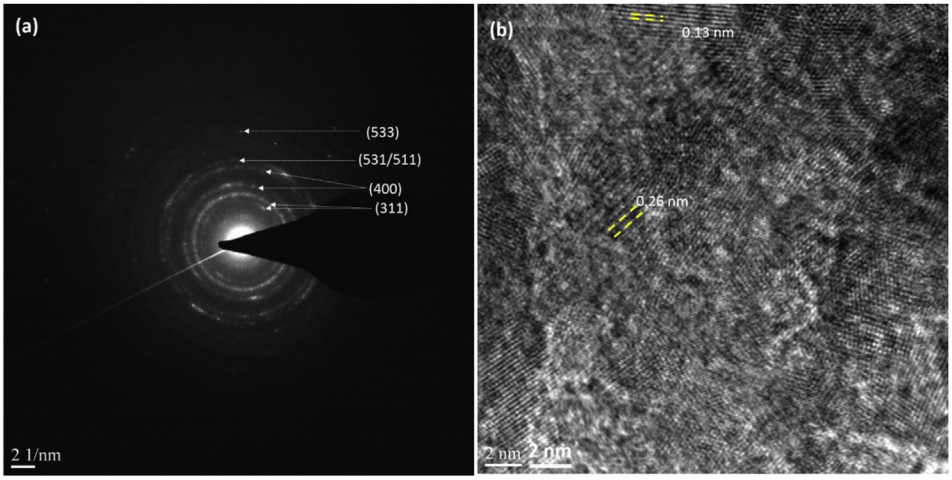

Fig. 4. (a) SAED pattern and (b) HR-TEM of NCS/O:4 composites of the $NiCo_2O_4/NiCo_2S_4$ sample.

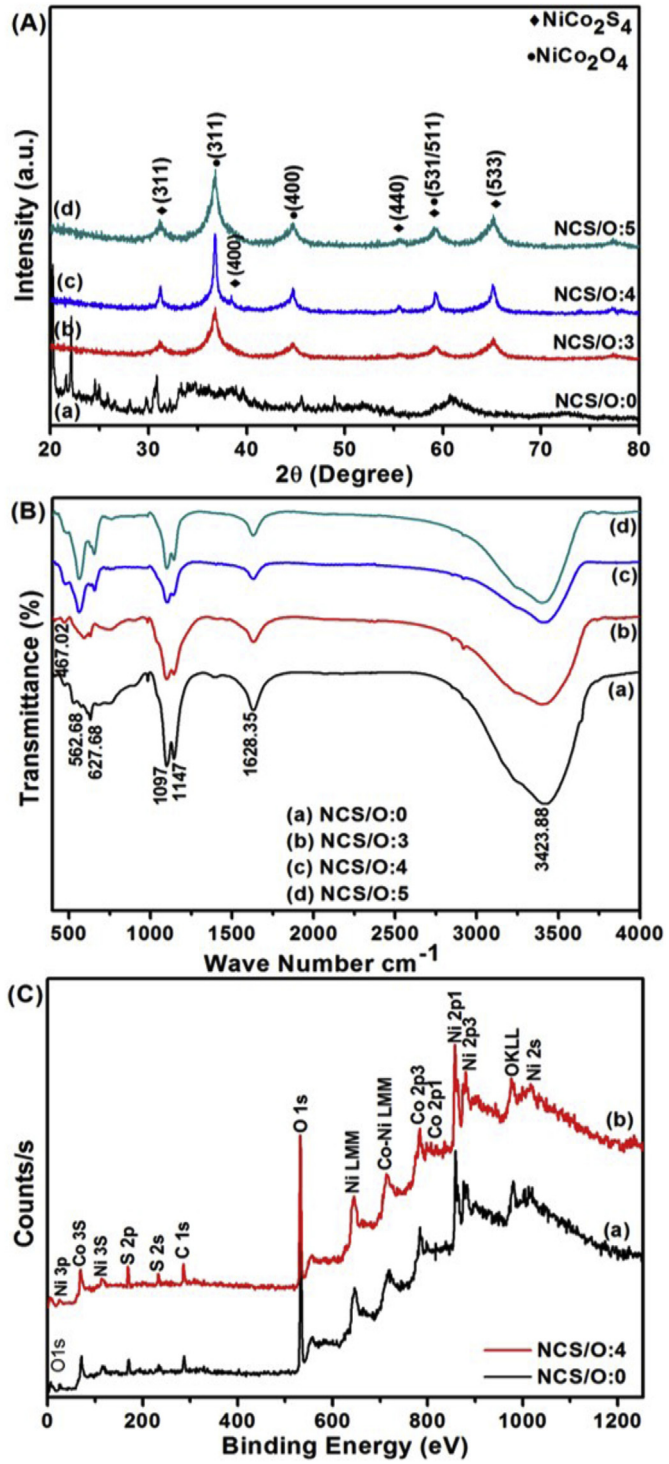

Fig. 5. (A) XRD patterns of (a) as-synthesized NCS/O:0, and annealed (b) NCS/O:3, (c) NCS/O:4, and (d) NCS/O:5 samples of the $NiCo_2O_4/NiCo_2S_4$ composites, **(B)** FT-IR spectra of the (a) as-synthesized NCS/O:0, and annealed (b) NCS/O:3, (c) NCS/O:4, and (d) NCS/O:5 samples of the $NiCo_2O_4/NiCo_2S_4$ composites prepared by the co-precipitation, **(C)** Survey spectra of (a) NCS/O:0, and (b) NCS/O:4 sample of the $NiCo_2O_4/NiCo_2S_4$ composite by the co-precipitation method, respectively.

formation of hybrid $NiCo_2S_4$ and $NiCo_2O_4$ nanomaterials. The sharp peaks located at 460, 477, 532, 656, 664 and 678 cm^{-1} correspond to the hybrid crystal structure of $NiCo_2S_4$ and $NiCo_2O_4$. We observed that the only the Ni–O/S and Co–O/S vibrational modes were identified from as-synthesized and annealed $NiCo_2S_4/NiCo_2O_4$ samples and no other vibration modes were observed [25,42]. All peaks strongly agree with the $T_{2g,3}$, E_g, $T_{2g,2}$, $T_{2g,1}$, and A_{1g} Raman modes of $NiCo_2O_4$ and $NiCo_2S_4$ [43]. From Figure S1b, the most intense peak at 664 cm^{-1} is related to the A_{1g} vibration mode of $NiCo_2S_4$, which suggests the successful formation of $NiCo_2S_4$ after annealing. From Raman analysis, we concluded that a pure phase of hybrid $NiCo_2O_4$ and $NiCo_2S_4$ was formed after annealing.

3.4. FT-IR spectroscopy analysis

Fourier transform infrared (FT-IR) spectroscopy is a well-known characterization technique for detailed studies of the functional groups of as-synthesized samples. Fig. 5B (a) shows the $NiCo_2O_4/NiCo_2S_4$ composite prepared by the co-precipitation method. Fig. 5B (b–d) shows the FT-IR spectrum of $NiCo_2O_4/NiCo_2S_4$ composite prepared at different Ni and Co ratios using the co-precipitation method and annealing at 300 °C. The peaks at 467.02, 562.68 and 627.68 cm^{-1} are assigned to the NiCo–S and NiCo–O bonding vibrations [44]. The peaks at 1097 and 1147 cm^{-1} are related to the stretching vibration of the C–N bond, which is reported in the literature [43–45]. The peak at 1628.35 cm^{-1} corresponds to bonds of the C–C fundamental vibration groups. The peaks at 2920 and 2852 cm^{-1} are related to the N–H bond [46], and the peak at 3423.88 cm^{-1} is ascribed to the existence of the O–H group in as-synthesized and annealed $NiCo_2O_4/NiCo_2S_4$ samples [40].

3.5. XPS analysis

XPS was used to evaluate the chemical and elemental states of Ni, Co, S, and O in the as-synthesized and annealed $NiCo_2O_4/NiCo_2S_4$ composites. Fig. 5C shows the survey spectra of as-synthesized and annealed $NiCo_2O_4/NiCo_2S_4$ composites produced by the co-precipitation method. From the survey spectra, we observed that Ni, Co, O, and S elements are present in all samples, which indicates the formation of hybrid $NiCo_2O_4/NiCo_2S_4$ composites material. No other impurity peaks were observed. Fig. 6(a–d) shows the core level spectrum of the Ni 2p, Co 2p, S 2p and O 1s regions of all samples, respectively. Fig. 6a shows the high-resolution spectrum of the Ni 2p regions of the $NiCo_2O_4/NiCo_2S_4$ composites samples as-prepared and NCS/O:4. The core level of the Ni 2p peaks shows the divalent Ni $2p_{3/2}$ and Ni $2p_{1/2}$ peaks at 855.94 eV and 873.49 eV, respectively. The two peaks observed at 880.26 eV and 861.25 eV related to the trivalent states of Ni 2p [47–49]. Fig. 6b displays the core level spectrum of the Co 2p element, which shows the doublets enclosing at bonding energy 780.59 and 796.14 eV of Co $2p_{3/2}$ and Co $2p_{1/2}$, respectively, consistent with the results reported elsewhere [47]. The splitting difference between the lower binding energy and the higher binding energy is 15.55 eV, which indicates that the Co^{2+} and Co^{3+} states are present in the samples. These types of results were reported previously [48]. After careful observation, Ni^{3+} was much lower than Ni^{2+}, which suggested that divalent states were formed in the $NiCo_2O_4/NiCo_2S_4$ composite. Fig. 6c represents the S 2p high-resolution spectra. The spectra of S 2p shows peaks at 168 eV, which suggests that S^{2-} is present while another small peak at 169.63 eV can be assigned to inorganic sulfates. Although sulfides can be distinguished from sulfates by their S 2p binding energy, sulfates and bisulfates show no significant difference in the S 2p region (the S 2p binding energies vary between 168.1 and 168.6 eV) [50]. Fig. 6d shows the high-resolution spectra of O 1s. The high-resolution spectra of O 1s shows the two peaks at 529 and 532.16 eV. The existence of a small peak at 529 eV, which is a characteristic of metal – oxygen binding. This is suggested to the lattice oxygen presented. A secondary strong peak appeared at 532.16 eV in Fig. 6d and is maybe due to the chemisorption oxygen [26,48]. Our XPS results proved that both oxygen and sulfur were present, which indicates the hybrid phase of $NiCo_2O_4/NiCo_2S_4$ was formed. According to the XPS studies, the $NiCo_2O_4/NiCo_2S_4$ composite contains Ni 2p, Co 2p, S 2p, and O 1s,

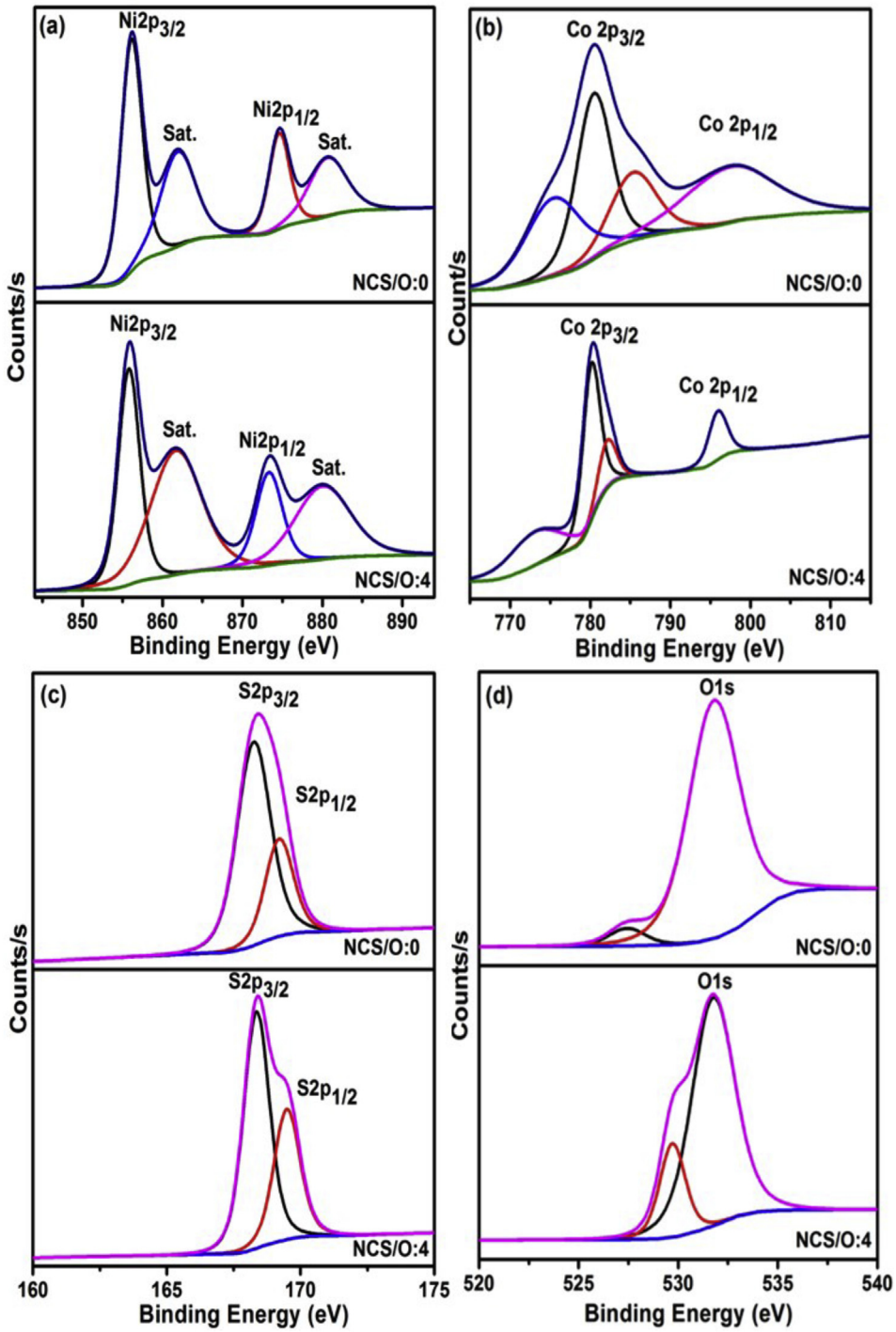

Fig. 6. Core level spectrum of the NCS/O:0, and (b) NCS/O:4 samples (a) Ni 2p, (b) Co 2p, (c) S 2p and (d) O 1s regions of the $NiCo_2O_4/NiCo_2S_4$ composite samples, respectively.

which is in a good composition with the hybrid phase of $NiCo_2O_4/NiCo_2S_4$ [49–52].

3.6. Electrochemical testing

To determine the supercapacitor performance of hybrid $NiCo_2O_4/NiCo_2S_4$ electrode, we next study the electrochemical properties of three different hybrid $NiCo_2O_4/NiCo_2S_4$ electrodes, labeled as NCS/O:3, NCS/O:4, and NCS/O:5, obtained with three different percentages of Ni and Co precursors, as shown in Fig. 7(a–c). Fig. 7(a–c) displays the CV curves of the NCS/O:3, NCS/O:4, and NCS/O:5 electrodes at 5–100 mV s^{-1} in 2 M KOH electrolyte, respectively. From Fig. 7(a–c), we observed that all CV curves had significant reduction and oxidation peaks at 0.25 V and −0.35 V, respectively that indicates the faradaic type of supercapacitive property of the hybrid $NiCo_2O_4/NiCo_2S_4$ active electrodes [51]. As the scan rate increases from 5 to 100 mV s^{-1}, the current densities increase up to 80 mA cm^{-2}. The reduction and oxidation peaks are shifted towards the positive and negative potential, respectively [26,53]. Out of these three samples, sample NCS/O:4 shows the highest current density at different scan rates from 5 to 100 mV s^{-1}; sample NCS/O:4 provided a higher reactive area during the electrochemical testing. Fig. 7b shows characteristic CV curves of

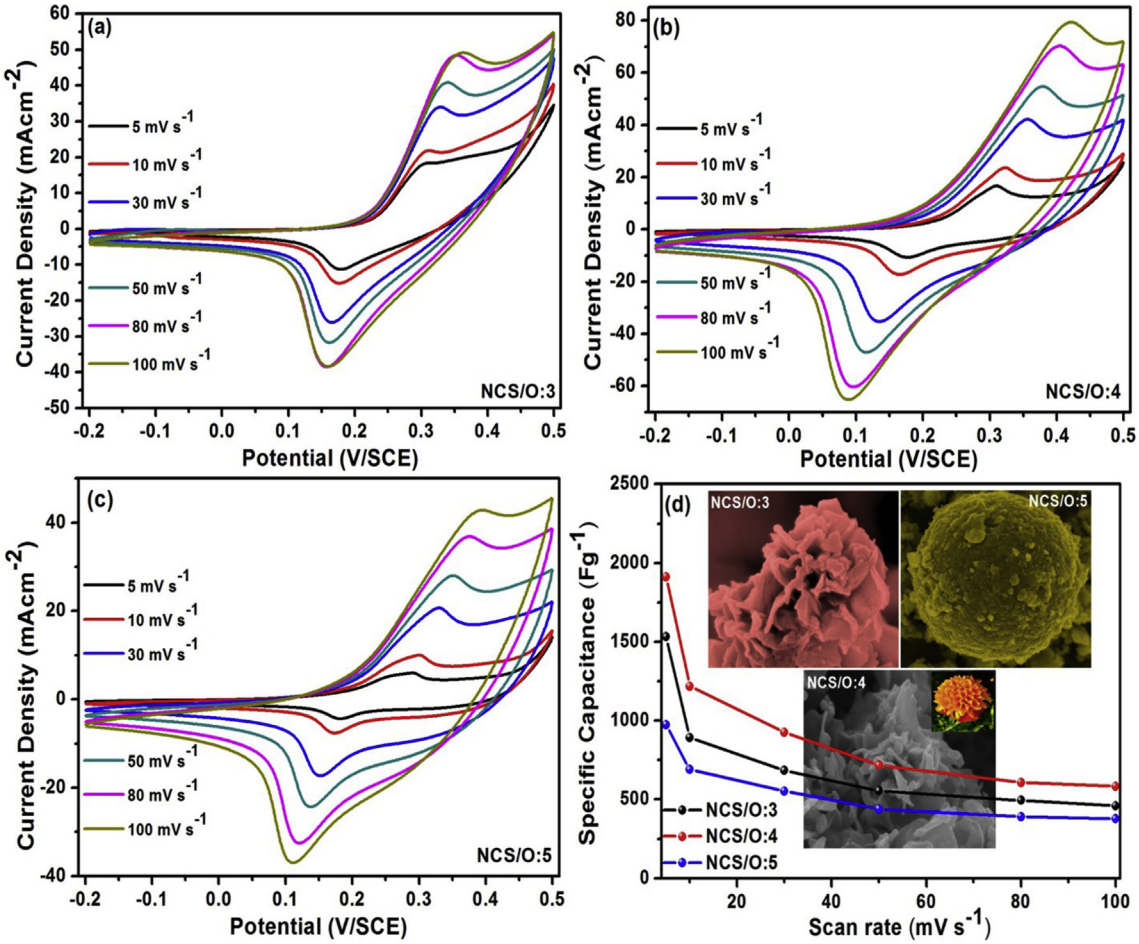

Fig. 7. (a–c) Cyclic voltammogram (CV) curves of the NCS/O:3, NCS/O:4, and NCS/O:5 electrodes at 5–100 mV s^{-1} in 2 M KOH electrolyte, respectively., (d) Specific capacitance of the NCS/O:3, NCS/O:4, and NCS/O:5 electrodes at 5–100 mV s^{-1} and inset shows the FESEM images.

the NCS/O:4 sample in 2 M KOH electrolyte with the −0.2 − 0.5 V potential window at different scan rates. Fig. 7b shows the increasing scan rate as current densities increases constantly up to 80 mA cm^{-2}. From Fig. 7, we clearly observed that the peak position of the oxidation and reduction are moving to positive and negative potentials, respectively, indicating fast-redox reactions during the electrode and electrolyte interfaces [54]. Fig. 7d displays the specific capacitance of the NCS/O:3, NCS/O:4, and NCS/O:5 electrodes at 5–100 mV s^{-1}. Fig. 7d indicates that the specific capacitance decreases with increase in scan rate. The specific capacitance of NCS/O:3, NCS/O:4, and NCS/O:5 electrodes can be calculated as 1556, 1966, and 1004 Fg^{-1} at a 5 mV s^{-1} scan rate, respectively. The resultant value of specific capacitance show that the NCS/O:4 electrode had the highest value of specific capacitance, the calculated values of specific capacitance of the NCS/O:4 electrode were 1966, 1221, 917, 707, 609, and 579 F g^{-1}, indicates that the NCS/O:4 electrode is suitable for the supercapacitor application. Because of nanoflakes-like nanostructures provided a higher surface reactive area and faster ion process in the electrochemical testing [50–54].

For further details on the electrochemical activities of hybrid samples, we used the GCD measurement and specific capacitance evolution. Fig. 8a shows the GCD curve of NCS/O:3, NCS/O:4, and NCS/O:5 electrodes at current densities 16 mA cm^{-2} with a −0.2–0.5 V potential window in the 2 M KOH electrolyte. The charge/discharge time of the NCS/O:3, NCS/O:4, and NCS/O:5 electrodes are 649.65, 1320.90, and 1036.5 s, at 16 mA cm^{-2} respectively. These results suggest that NCS/O:4 shows the highest discharging time compared to the other two electrodes. This indicates that sample NCS/O:4 shows the highest specific capacitance compared to NCS/O:3, and NCS/O:5 (shows in Fig. 8b), which could be due to the contribution of uniform formation and porous nanoflakes-like nanostructure with a higher active surface area providing a larger number of ions and the motion of the ions is very fasts [52–55]. Fig. 8c displays the charge/discharge curve of NCS/O:4 electrodes at different current densities from 16 to 42 mA cm^{-2} in the −0.2 − 0.5 V potential window. From Fig. 8c, we see that as current density increases, discharge time decreases, which corresponds to a faradic reaction [51,52]. The specific capacitance was calculated using a standard formula. Fig. 8d shows the specific capacitance with respect to the different current densities. The calculated values of specific capacitance of NCS/O:4 sample is 1988.6, 1668.9, 1549.7, 1512.66, 1371.4, 1182.9, 1152.9, and 1020.56 F g^{-1} at current densities of 16–42 mA cm^{-2}, respectively. Also, the value of specific capacitance for samples NCS/O:3 and NCS/O:5 were calculated and shown in Fig. 8b. Fig. 8(a and b) indicates that sample NCS/O:4 was the superior electrode for supercapacitor applications [56]. The cyclic performance of an optimized $NiCo_2O_4/NiCo_2S_4$ electrode was tested in the 2 M KOH at 100 mV s^{-1} for 5000 cycles, as shown in Fig. 8e. Fig. 8e inset shows the CV curve of NCS/O:3, NCS/O:4, and NCS/O:5 electrodes at cycle 1, 2 and 5000 respectively. The calculated value of specific capacitance of the $NiCo_2O_4/NiCo_2S_4$ electrode shows that the value of specific capacitance is maintained, even after 1000 cycles, with 91% capacity retention shown in Fig. 8e.

3.7. Electrochemical impedance spectroscopy (EIS) analysis

EIS analysis was used to further study the electrochemical

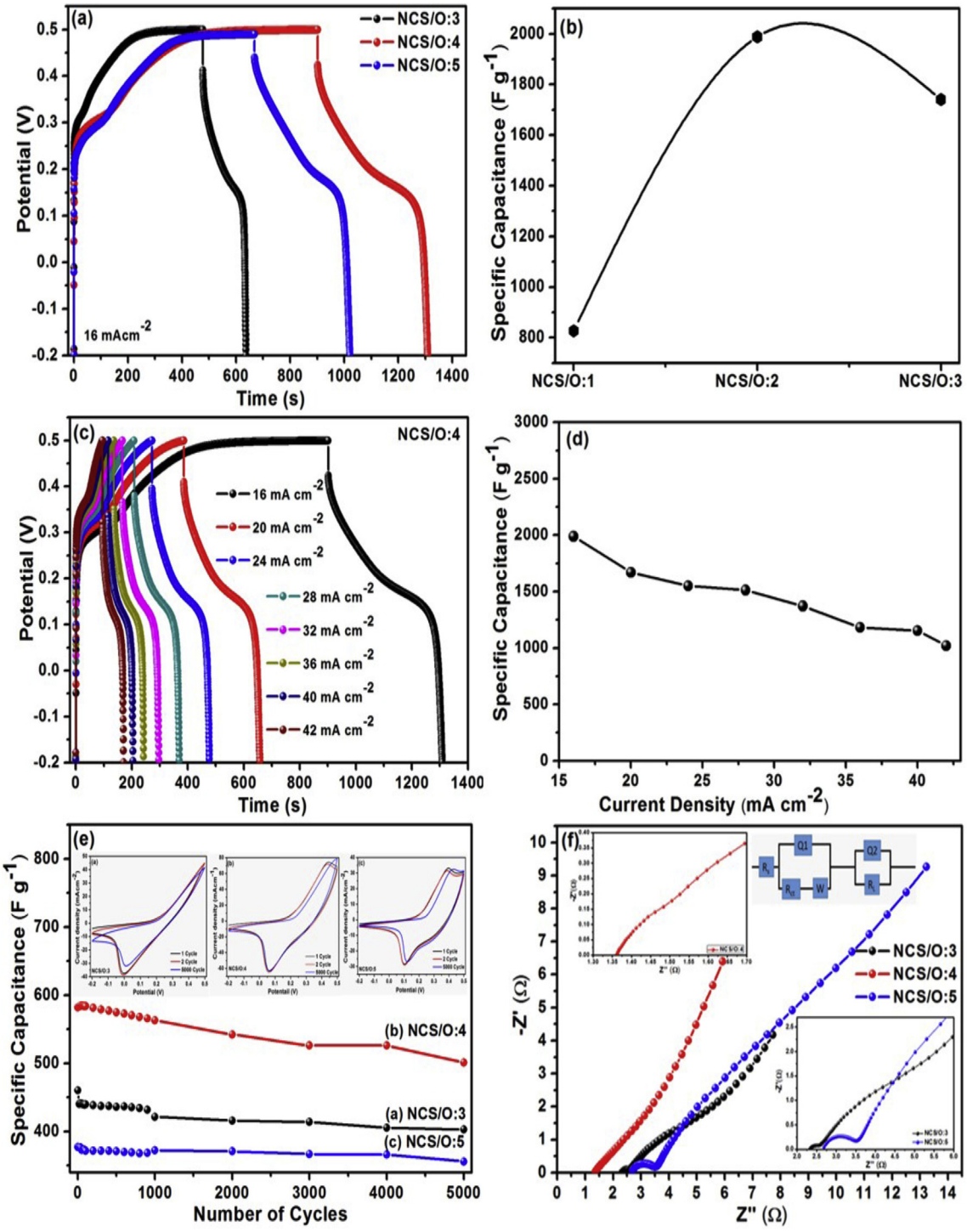

Fig. 8. (a, b) GCD curve and specific capacitance of NCS/O:3, NCS/O:4, and NCS/O:5 electrodes at current densities 16 mA cm^{-2} with a −0.2–0.5 V potential window in the 2 M KOH electrolyte, respectively, (c) Charge/discharge curve of NCS/O:4 electrodes at different current densities from 16 to 42 mA cm^{-2} in the −0.2 − 0.6 V potential window, and (d) Specific capacitance with respect to the different current densities from 16 to 42 mA cm^{-2} of the NCS/O:4 sample, (e) Capacity retention with cycle number of the NCS/O:3, NCS/O:4, and NCS/O:5 electrodes, and inset shows the CV curve of NCS/O:3, NCS/O:4, and NCS/O:5 electrodes at cycle 1, 2 and 5000 respectively, (f) Nyquist plots of the NCS/O:3, NCS/O:4, and NCS/O:5 and the inset shows the high scale figure and equivalent circuit.

mechanism of composite electrodes. The EIS spectra of the NCS/O:3, NCS/O:4, and NCS/O:5 electrodes are shown in Fig. 8f. Fig. 8f shows the Nyquist plots of the NCS/O:3, NCS/O:4, and NCS/O:5 electrodes in a high range of 1 and 100 kHz at open circuit potential and the inset shows the equivalent circuit. In the Nyquist plots, one small semicircle was appeared, it may be related to charge-transfer resistance during the electrolyte/electrode interface [37,56]. Table 1 depicts the values of solution resistance (R_s) and charge transfer resistance (R_{ct}) for NCS/O:3, NCS/O:4, and NCS/O:5 electrodes. Obviously, the R_s and R_{ct} of the hybrid NCS/O:4 electrode is lower than the NCS/O:3, NCS/O:5, electrode, because of NCS/O:4 sample provided higher surface area and porous area. This suggests that the nanoflake-like NCS/O:4 electrode is

Table 1
EIS parameters of $NiCo_2O_4/NiCo_2S_4$ electrodes synthesized co-precipitation method.

Parameters	NCS/O:3	NCS/O:4	NCS/O:5
$R_{s\ (\Omega)}$	2.35	2.26	2.80
$R_{ct\ (\Omega)}$	6.40	0.64	13.48
W	0.22	0.050	0.48
C	0.14	0.074	0.29
$R_{1\ (\Omega)}$	0.69	1.42	21.96

more conductive, which is very useful for supercapacitor applications as an energy storage material [50,51].

3.8. Symmetric fabrication and device performance

Fig. 9a presents the CV curves of the symmetric supercapacitor, using the as-prepared NCS/O:4 electrodes as the positive and negative electrodes as a function of different scan rates. The working window is 0.0–0.7 V. Fig. 9b shows the variation of specific capacitance with respect to the different scan rates, ranging from 5 to 100 mV s^{-1}, revealing that as the scan rate increases, the specific capacitance decreases. The resultant specific capacitance values were calculated as 130, 100, 74, 66, 60, and 56 F g^{-1} at the scan rates of 5, 10, 30, 50, 80, and 100 mV s^{-1}, respectively. Fig. 9(c and d) illustrate the galvanostatic discharge curves and specific capacitance at different current

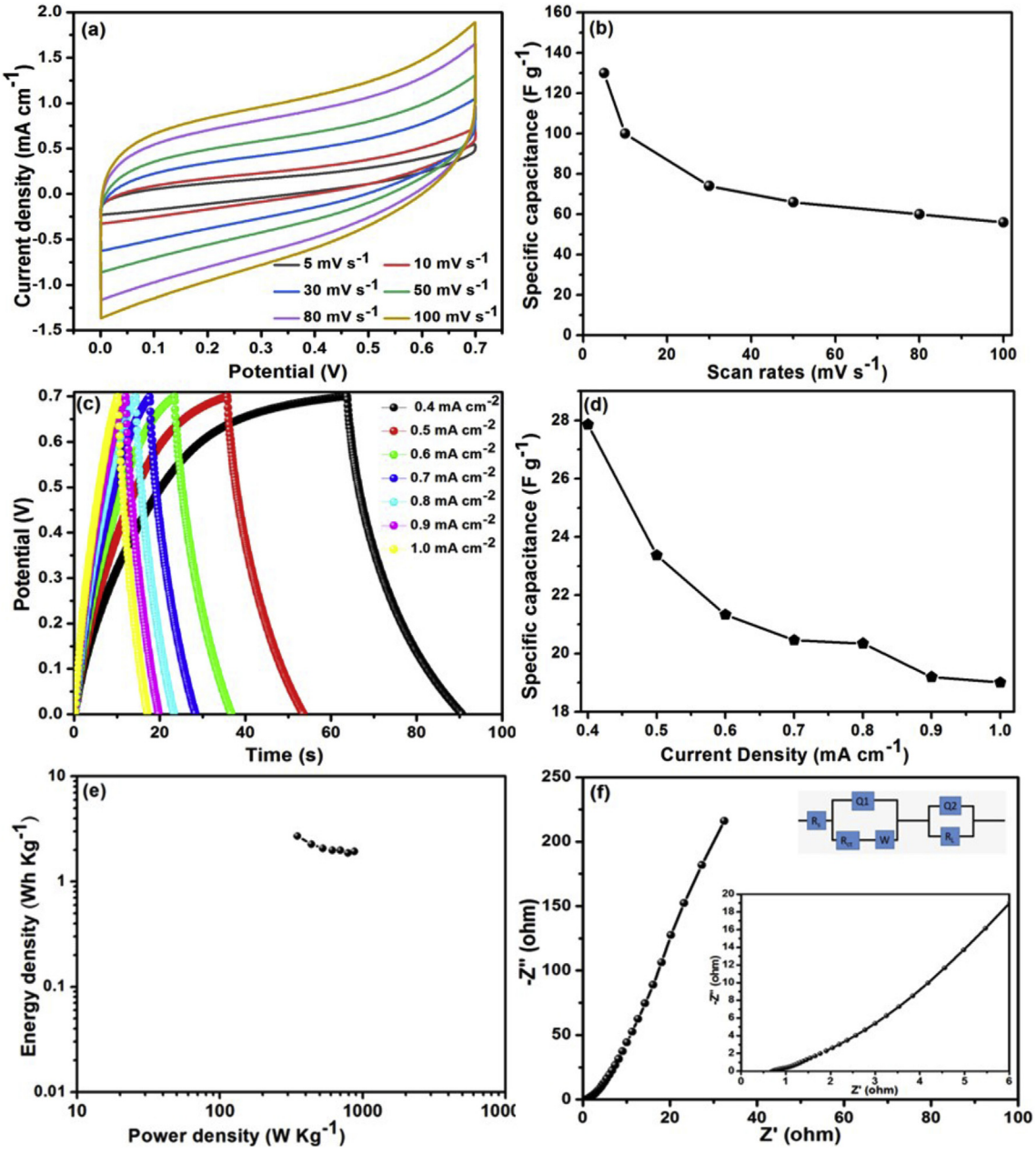

Fig. 9. (a) CV curves of NCS/O:4 symmetric supercapacitor (SC) at various scan rate from 5 to 100 mVs^{-1}, (b) Specific capacitance with respect to the different scan rates of the NCS/O:4 symmetric supercapacitor, (c) Charge-discharge curves at various current densities, (d) Specific capacitance with respect to the different current densities from 0.4 to 1 mA cm^{-2} in the positive window 0–0.7 V, (e) Ragone plot of the SC device, (f) Nyquist plots of the symmetric SC and the inset shows equivalent circuit.

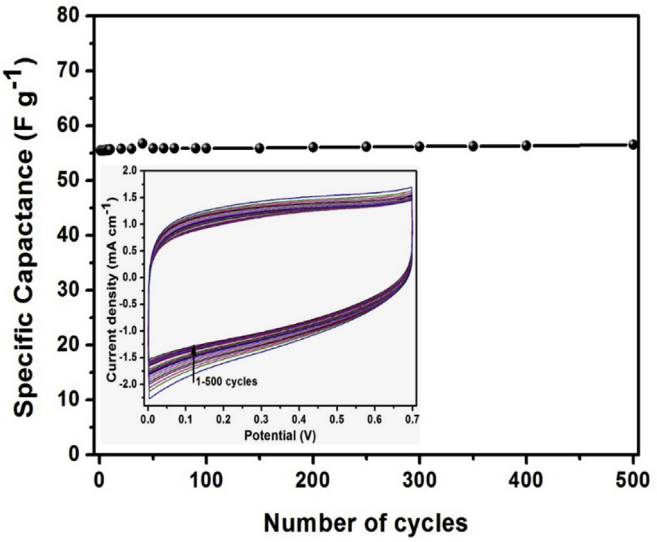

Fig. 10. Cycling stability of the SC device with respect to the CV cycles.

density, respectively. The calculated specific capacitance values were 28, 23, 21, 20, 19, and 18 F g^{-1} at the current densities of 0.4–1 mA cm^{-2}, respectively [57]. Fig. 9 (e, f) shows the Ragone plot and EIS curve of NCS/O:4 electrode, respectively. This suggest the $NiCo_2O_4/NiCo_2S_4$ hybrid electrode is a better electrode for the asymmetric supercapacitor application. Fig. 10 shows the cycling stability of the optimized NCS/O:4 electrode, which indicates the $NiCo_2O_4/NiCo_2S_4$ hybrid electrode is very suitable for the asymmetric device fabrication.

4. Conclusions

In this paper, we successfully synthesized nanoflake-, flower-, and spherical-like nanostructure $NiCo_2O_4/NiCo_2S_4$ by a co-precipitation and screen-printing methods to obtain improved electrochemical performance for supercapacitors. The diameter of nanoflowers and nanospheres are around 1 and 2.5 μm for $NiCo_2O_4/NiCo_2S_4$ electrodes prepared using co-precipitation, respectively. The effect of Ni and Co on $NiCo_2O_4/NiCo_2S_4$ electrodes exhibited outstanding supercapacitor performance with excellent stability. The $NiCo_2O_4/NiCo_2S_4$ electrodes showed the specific capacitance of NCS/O:3, NCS/O:4, and NCS/O:5 were 1556, 1966, and 1004 Fg^{-1} at 5 mV s^{-1}, respectively. Therefore, we concluded that $NiCo_2O_4/NiCo_2S_4$ flower-like nanostructures are capable electrodes for supercapacitor applications and devices fabrication.

Acknowledgment

This work was supported by the Dongguk University Research Fund of 2018.

Appendix A. Supplementary data

Supplementary data to this article can be found online at https://doi.org/10.1016/j.ceramint.2019.05.274.

References

[1] D.P. Dubal, O. Ayyad, V. Ruiz, P. Gomez-Romero, Hybrid energy storage: the merging of battery and supercapacitor chemistries, Chem. Soc. Rev. 44 (2015) 1777–1790.
[2] H. Khani, D.O. Wip, Iron oxide nanosheets and pulse-electrodeposited Ni-Co-S nanoflake arrays for high-performance charge storage, ACS Appl. Mater. Interfaces 9 (2017) 6967–6978.
[3] S.R. Peurifoy, J.C. Russell, T.J. Sisto, Y. Yang, X. Roy, C. Nuckolls, Designing three-dimensional architectures for high-performance electron accepting pseudocapacitors, J. Am. Chem. Soc. 140 (2018) 10960–10964.
[4] B.E. Conway, V. Birss, J. Wojtowicz, The role and utilization of pseudocapacitance for energy storage by supercapacitors, J. Power Sources 66 (1997) 1–14.
[5] H. Mei, Y. Mei, S. Zhang, Z. Xiao, B. Xu, H. Zhang, L. Fan, Z. Huang, W. Kang, D. Sun, Bimetallic-MOF derived accordion-like ternary composite for high performance supercapacitors, Inorg. Chem. 57 (2018) 10953–10960.
[6] G. Wang, L. Zhang, J. Zhang, A review of electrode materials for electrochemical supercapacitors, Chem. Soc. Rev. 41 (2012) 797–828.
[7] Y. Wang, B. Shang, F. Lin, Y. Chen, R. Ma, B. Peng, Z. Deng, Controllable synthesis of hierarchical nickel hydroxide nanotubes for high performance supercapacitors, Chem. Commun. 54 (2018) 559–562.
[8] S. Gao, Y. Sun, F. Lei, L. Liang, J. Liu, W. Bi, B. Pan, Y. Xie, Ultrahigh energy density realized by a single-layer β-$Co(OH)_2$ all-solid-state asymmetric supercapacitor, Angew. Chem. Int. Ed. 53 (2014) 12789–12793.
[9] X. Sun, G. Wang, H. Sun, F. Lu, M. Yu, J. Lian, Morphology controlled high performance supercapacitor behavior of the Ni-Co binary hydroxide system, J. Power Sources 238 (2013) 150–156.
[10] J. Yan, Z. Fan, W. Sun, G. Ning, T. Wei, Q. Zhang, R. Zhang, L. Zhi, F. Wei, Advanced asymmetric supercapacitors based on $Ni(OH)_2$/Graphene and porous graphene electrodes with high energy density, Adv. Funct. Mater. 22 (2012) 2632–2641.
[11] H. Pang, X. Li, Q. Zhao, H. Xue, W.-Y. Lai, Z. Hu, W. Huang, One-pot synthesis of heterogeneous Co_3O_4-nanocube/$Co(OH)_2$-nanosheet hybrids for high-performance flexible asymmetric all-solid state supercapacitors, Nanomater. Energy 35 (2017) 138–145.
[12] K.-L. Yan, X. Shang, Z. Li, B. Dong, J.-Q. Chi, Y.-R. Liu, W.-K. Gao, Y.-M. Chai, C.-G. Liu, Facile synthesis of binary NiCoS nanorods supported on nickel foam as efficient electrocatalysts for oxygen evolution reaction, Int. J. Hydrogen Energy 42 (2017) 17129–17135.
[13] J. Xu, L. Zhang, G. Xu, Z. Sun, C. Zhang, X. Ma, C. Qi, L. Zhang, D. Jia, Facile synthesis of NiS anchored carbon nanofibers for high-performance supercapacitors, Appl. Surf. Sci. 434 (2018) 112–119.
[14] Y. Ning, D. Ma, Y. Shen, F. Wang, X. Zhang, Constructing hierarchical mushroom-like bifunctional NiCo/$NiCo_2S_4$@NiCo/Ni foam electrocatalysts for efficient overall water splitting in alkaline media, Electrochim. Acta 265 (2018) 19–31.
[15] L. Li, J. Wu, B. Liu, X. Liu, C. Li, Y. Gong, Y. Huang, L. Pan, NiS sheets modified CdS/reduced graphene oxide composite for efficient visible light photocatalytic hydrogen evolution, Catal. Today 315 (2018) 110–116.
[16] A. Sarkar, A.K. Chakraborty, S. Bera, NiS/rGO nanohybrid: an excellent counter electrode for dye sensitized solar cell, Sol. Energy Mater. Sol. Cell. 182 (2018) 314–320.
[17] X. Han, F. Liao, Y. Zhang, X. Han, C. Xu, H. Chen, Solvothermal preparation of zinc cobaltite mesoporous microspheres for high-performance electrochemical supercapacitors, J. Alloy. Comp. 781 (2019) 425–432.
[18] F. Liao, X. Han, Y. Zhang, X. Han, C. Xu, H. Chen, Hydrothermal synthesis of mesoporous $MnCo_2O_4/CoCo_2O_4$ ellipsoid-like microstructures for high-performance electrochemical supercapacitors, Ceram. Int. 45 (2019) 7244–7252.
[19] H. Chen, J. Wang, F. Liao, X. Han, C. Xu, Y. Zhang, Facile synthesis of porous Mn-doped Co_3O_4 oblique prisms as an electrode material with remarkable pseudocapacitance, Ceram. Int. 45 (2019) 8008–8016.
[20] Y. Liu, G. Jiang, S. Sun, B. Xu, J. Zhou, Y. Zhang, J. Yao, Decoration of carbon nanofibers with $NiCo_2S_4$ nanoparticles for flexible asymmetric supercapacitors, J. Alloy. Comp. 731 (2018) 560–568.
[21] T. Xiao, J. Li, X. Zhuang, W. Zhang, S. Wang, X. Chen, P. Xiang, L. Jiang, X. Tan, Wide potential window and high specific capacitance triggered via rough $NiCo_2S_4$ nanorod arrays with open top for symmetric supercapacitors, Electrochim. Acta 269 (2018) 397–404.
[22] X.-X. Li, X.-T. Wang, K. Xiao, T. Ouyang, N. Li, Z.-Q. Liu, In situ formation of consubstantial $NiCo_2S_4$ nanorods arrays toward self-standing electrode for high activity supercapacitors and overall water splitting, J. Power Sources 402 (2018) 116–123.
[23] Y. Liu, Z. Wang, Y. Zhong, M. Tade, W. Zhou, Z. Shao, Molecular design of mesoporous $NiCo_2O_4$ and $NiCo_2S_4$ with sub-micrometer-polyhedron architectures for efficient pseudo capacitive energy storage, Adv. Funct. Mater. 27 (2017) 1701229–1701239.
[24] S. Raj, S.K. Srivastava, P. Kar, P. Roy, Three-dimensional $NiCo_2O_4/NiCo_2S_4$ hybrid nanostructure on Ni-foam as a high-performance supercapacitor electrode, RSC Adv. 6 (2016) 95760–95767.
[25] L. Jinlong, L. Tongxiang, Y. Meng, S. Ken, M. Hideo, Performance comparison of $NiCo_2O_4$ and $NiCo_2S_4$ formed on Ni foam for supercapacitor, Compos. B Eng. 123 (2017) 28–33.
[26] H. Rong, T. Chen, R. Shi, Y. Zhang, Z. Wang, Hierarchical $NiCo_2O_4$@$NiCo_2S_4$ nanocomposite on Ni foam as an electrode for hybrid supercapacitors, ACS Omega 3 (2018) 5634–5642.
[27] S.K. Shinde, D.-Y. Kim, G.S. Ghodake, N.C. Maile, A.A. Kadam, D.S. Lee, M.C. Rath, V.J. Fulari, Morphological enhancement to CuO nanostructures by electron beam irradiation for biocompatibility and electrochemical performance, Ultrason. Sonochem. 40 (2018) 314–322.
[28] Z. Zhang, Q. Li, Z. Li, J. Ma, C. Li, L. Yin, X. Gao, Partially reducing reaction tailored mesoporous 3D carbon coated NiCo-$NiCoO_2$/Carbon xerogel hybrids as anode materials for lithium ion battery with enhanced electrochemical performance, Electrochim. Acta 203 (2016) 117–127.
[29] S.K. Shinde, D.P. Dubal, G.S. Ghodake, D.Y. Kim, V.J. Fulari, Nanoflower-like CuO/$Cu(OH)_2$ hybrid thin films: synthesis and electrochemical supercapacitive properties, J. Electroanal. Chem. 732 (2014) 80–85.

[30] D.-Y. Kim, G.S. Ghodake, N.C. Maile, A.A. Kadam, D.S. Lee, V.J. Fulari, S.K. Shinde, Chemical synthesis of hierarchical $NiCo_2S_4$ nanosheets like nanostructure on flexible foil for a high performance supercapacitor, Sci. Rep. 7 (2017) 9764–9774.
[31] J.-X. Feng, S.-H. Ye, X.-F. Lu, Y.-X. Tong, G.-R. Li, Asymmetric paper supercapacitor based on amorphous porous Mn_3O_4 negative electrode and $Ni(OH)_2$ positive electrode: a novel and high-performance flexible electrochemical energy storage device, ACS Appl. Mater. Interfaces 7 (2015) 11444–11451.
[32] J. Deng, H. Zhang, Y. Zhang, P. Luo, L. Liu, Y. Wang, Striking hierarchical urchin-like peapoded $NiCo_2O_4$@C as advanced bifunctional electrocatalyst for overall water splitting, J. Power Sources 372 (2017) 46–53.
[33] H. Liang, J. Lin, H. Jia, S. Chen, J. Qi, J. Cao, T. Lin, W. Fei, J. Feng, Hierarchical NiCo-LDH@NiOOH core-shell heterostructure on carbon fiber cloth as battery-like electrode for supercapacitor, J. Power Sources 378 (2018) 248–254.
[34] S.K. Shinde, G.S. Ghodake, D.P. Dubal, R.V. Patel, R.G. Saratale, D.-Y. Kim, N.C. Maile, R.R. Koli, H.D. Dhaygude, V.J. Fulari, Electrochemical synthesis: monoclinic Cu_2Se nano-dendrites with high performance for supercapacitors, J. Taiwan Inst. Chem. E. 75 (2017) 271–279.
[35] S.K. Shinde, G.S. Ghodake, D.P. Dubal, H.D. Dhaygude, D.-Y. Kim, V.J. Fulari, Enhanced photoelectrochemical properties of nanoflower-like hexagonal $CdSe_{0.6}Te_{0.4}$: effect of electron beam irradiation, J. Ind. Eng. Chem. 45 (2017) 92–98.
[36] L. Ma, Y. Hu, R. Chen, G. Zhu, T. Chen, H. Lv, Y. Wang, J. Liang, H. Liu, C. Yan, H. Zhu, Z. Tie, Z. Jin, J. Liu, Self-assembled ultrathin $NiCo_2S_4$ nanoflakes grown on Ni foam as high-performance flexible electrodes for hydrogen evolution reaction in alkaline solution, Nanomater. Energy 24 (2016) 139–147.
[37] D. Kong, W. Ren, C. Cheng, Y. Wang, Z. Huang, H.Y. Yang, Three-Dimensional $NiCo_2O_4$@Polypyrrole coaxial nanowire arrays on carbon textiles for high-performance flexible asymmetric solid state supercapacitor, ACS Appl. Mater. Interfaces 7 (2015) 21334–21346.
[38] F. Lu, M. Zhou, W. Li, Q. Weng, C. Li, Y. Xue, X. Jiang, X. Zeng, Y. Bando, D. Golberg, Engineering sulfur vacancies and impurities in $NiCo_2S_4$ nanostructures toward optimal supercapacitive performance, Nanomater. Energy 26 (2016) 313–323.
[39] C. Chen, D. Yan, X. Luo, W. Gao, G. Huang, Z. Han, Y. Zeng, Z. Zhu, Construction of core-shell $NiMoO_4$@Ni-Co-S nanorods as advanced electrodes for high-performance asymmetric supercapacitors, ACS Appl. Mater. Interfaces 10 (2018) 4662–4671.
[40] M. Yan, Y. Yao, J. Wen, L. Long, M. Kong, G. Zhang, X. Liao, G. Yin, Z. Huang, Construction of a hierarchical $NiCo_2S_4$@ppy core−shell heterostructure nanotube array on Ni foam for a high-performance asymmetric supercapacitor, ACS Appl. Mater. Interfaces 8 (2016) 24525–24535.
[41] Z. Wu, P. Li, Q. Qin, Z. Li, X. Liu, N-doped graphene combined with alloys (NiCo, CoFe) and their oxides as multifunctional electrocatalysts for oxygen and hydrogen electrode reactions, Carbon 139 (2018) 35–44.
[42] S.K. Shinde, M.B. Jalak, G.S. Ghodake, N.C. Maile, V.S. Kumbhar, D.S. Lee, V.J. Fulari, D.-Y. Kim, Chemically synthesized nanoflakes-like $NiCo_2S_4$ electrodes for high-performance supercapacitor application, Appl. Surf. Sci. 466 (2019) 822–829.
[43] C. Xia, P. Li, J. Li, Q. Jiang, X. Zhang, H.N. Alshareef, General top-down ion exchange process for the growth of epitaxial chalcogenide thin films and devices, Chem. Mater. 29 (2017) 690–698.
[44] S. Raj, Y. Dong, P. Kar, L. Mai, S. Jin, P. Roy, Hybrid $NiCo_2O_4$-$NiCo_2S_4$ nanoflakes as high-performance anode materials for lithium-ion batteries, Chem. Select. 3 (2018) 2315–2320.
[45] J. Hou, Y. Sun, Y. Wu, S. Cao, L. Sun, Promoting active sites in core–shell nanowire array as mott-Schottky electrocatalysts for efficient and stable overall water splitting, Adv. Funct. Mater. 28 (2018) 1704447–1704459.
[46] D.P. Dubal, S. Patil, A.D. Jagadale, C.D. Lokhande, Two step novel chemical synthesis of polypyrrole nanoplates for supercapacitor application, J. Alloy. Comp. 509 (2011) 8183–8188.
[47] D. Yao, Y. Ouyang, X. Jiao, H. Ye, W. Lei, X. Xia, L. Lu, Q. Hao, Hierarchical NiO@$NiCo_2O_4$ electrochemical supercapacitors, core−shell nanosheet arrays on Ni foam for high-performance, Ind. Eng. Chem. Res. 57 (2018) 6246–6256.
[48] J. Xiao, L. Wan, S. Yang, F. Xiao, S. Wang, Design hierarchical electrodes with highly conductive $NiCo_2S_4$ nanotube arrays grown on carbon fiber paper for high performance pseudocapacitors, Nano Lett. 14 (2014) 831–838.
[49] L. Su, L. Gao, Q. Du, L. Hou, X. Yin, M. Feng, W. Yang, Z. Ma, G. Shao, Formation of micron-sized nickel cobalt sulfide solid spheres with high tap density for enhancing pseudocapacitive properties, ACS Sustain. Chem. Eng. 5 (2017) 9945–9954.
[50] A.A. Audi, P.M.A. Sherwood, X-ray photoelectron spectroscopic studies of sulfates and bisulfates interpreted by Xα and band structure calculations, Surf. Interface Anal. 29 (2000) 265–275.
[51] X. Chen, D. Chen, X. Guo, R. Wang, H. Zhang, Facile growth of caterpillar-like $NiCo_2S_4$ nanocrystal arrays on nickle foam for high-performance supercapacitors, ACS Appl. Mater. Interfaces 9 (2017) 18774–18781.
[52] X. Xu, H. Zhao, J.K. Zhou, R. Xue, J. Gao, $NiCoO_2$ flowers grown on the aligned-flakes coated Ni foam for application in hybrid energy storage, J. Power Sources 329 (2016) 238–246.
[53] C. Cui, J. Xu, L. Wang, D. Guo, M. Mao, J. Ma T. Wang, Growth of $NiCo_2O_4$@$MnMoO_4$ nanocolumn arrays with superior pseudocapacitor properties, ACS Appl. Mater. Interfaces 8 (2016) 8568–8575.
[54] S. Zhang, W. Su, K. Li, D. Liu, J. Wang, P. Tian, Metal organic framework-derived Co_3O_4/$NiCo_2O_4$ double-shelled nanocage modified activated carbon air-cathode for improving power generation in microbial fuel cell, J. Power Sources 396 (2018) 355–362.
[55] X. Liu, S. Shi, Q. Xiong, L. Li, Y. Zhang, H. Tang, C. Gu, X. Wang, J. Tu, Hierarchical $NiCo_2O_4$@$NiCo_2O_4$ core/shell nanoflake arrays as high performance supercapacitor materials, ACS Appl. Mater. Interfaces 5 (2013) 8790–8795.
[56] R. Li, S. Wang, Z. Huang, F. Lu, T. He, $NiCo_2S_4$@$Co(OH)_2$ core-shell nanotube arrays in situ grown on Ni foam for high performances asymmetric supercapacitors, J. Power Sources 312 (2016) 156–164.
[57] J.S. Chen, C. Guan, Y. Gui, D.J. Blackwood, Rational design of self-supported Ni_3S_2 nanosheets array for advanced asymmetric supercapacitor with a superior energy density, ACS Appl. Mater. Interfaces 9 (2017) 496–504.